Applied Catalysis B: Environment and Energy 383 (2026) 126035

Contents lists available at ScienceDirect

Applied Catalysis B: Environment and Energy

journal homepage: www.elsevier.com/locate/apcatb

Grain boundary segregation engineering in high-entropy multiphase alloys for overall water splitting at ultra-high current density

YiFan Cui [a,b,c,d], YongHui Wang [a,d,e], Bo Li [a,d], Yu Sui [b,e], Gang Wang [f], JunTao Huo [g], JianHua Li [h], JiaQi Huang [a,d], Yan Du [a,b,d], ZhenWen Yu [a,d], JianFei Sun [a,d], SiDa Jiang [a,b,c,d,*]

[a] School of Materials Science and Engineering, Harbin Institute of Technology, Harbin 150001, China
[b] Laboratory for Space Environment and Physical Sciences, Harbin Institute of Technology, Harbin 150001, China
[c] Frontier Science Center for Interaction between Space Environment and Matter, and National Key Laboratory of Space Environment and Matter Behaviors, China
[d] National Key Laboratory for Precision Hot Forming, Harbin Institute of Technology, Harbin 150001, China
[e] School of Physics, Harbin Institute of Technology, Harbin 150001, China
[f] Laboratory for Microstructures, Institute of Materials, Shanghai University, Shanghai 20044, China
[g] Key Laboratory of Magnetic Materials and Devices, and Zhejiang Province Key Laboratory of Magnetic Materials and Application Technology, Ningbo Institute of Materials Technology and Engineering, Chinese Academy of Sciences, Ningbo 315201, China
[h] Beijing Engineering Research Center of Detection and Application for Weak Magnetic Field, Department of Physics, University of Science and Technology Beijing, Beijing 100083, China

ARTICLE INFO

Keywords:
Water splitting
Industrial current density
High entropy alloys
Grain boundary segregation engineering
Heterostructural regulation

ABSTRACT

In industrial water splitting, alkaline electrolyzers demonstrate promising development prospects due to lower costs and enhanced safety. However, for anion-exchange membrane (AEM) systems, require high current densities (> 2 A cm^{-2}) to optimize energy utilization efficiency. High-entropy alloys (HEAs) have recognized as viable electrocatalysts for water splitting owing to their exceptional activity and cost-effectiveness. However, their complex composition design and practical application at ultra-high industrial current density remains a significant challenge. Herein, we develop a theoretical and experimental approach combined efficient component screening and heterostructure regulation to improve the oxygen evolution reaction (OER) activity and stability at ultra-high current density in high-entropy multiphase alloys, leveraging machine learning (ML) techniques and grain boundary segregation engineering (GBSE). The $Fe_{20}Co_{20}Ni_{20}Mo_{20}Cu_{15}Al_5$ electrocatalyst, synthesized via a melt-extraction method and exhibiting intrinsic self-supporting properties, demonstrated outstanding OER performance with an overpotential (η) of 370@1 A cm^{-2} and 497 mV@3 A cm^{-2}, while maintained stability for approximately 800 and 95 h. A notable achievement is that the voltage of electrolyzer is approximately 1.90 V at current density of 0.5 A cm^{-2} with stable operation for 100 h when using the $Fe_{20}Co_{20}Ni_{20}Mo_{20}Cu_{15}Al_5$ as both anode and cathode for overall water splitting in an AEM electrolyzer. The mixing enthalpy and prepared method facilitates Cu grain boundary segregation, enhancing both the activity of Ni sites and the overall conductivity. These findings offer a practicable HEAs design strategy for catalysis that realizes the manipulation of active sites on atomic scale and underscore the potential of HEAs for industrial-scale applications in water splitting.

1. Introduction

Water splitting for hydrogen production represents a pivotal pathway to address the ongoing energy crisis [1–4]. Significant advancements have been made in recent years to reduce the overpotential (η) and minimize the use of noble metals in electrocatalysts [5–9]. These developments span various materials, including oxides [10–12], hydroxides [13,14], and transition metal alloys [15–17]. For industrial application, noble metals achieve high activity and stability in proton exchange membrane water electrolysis (PEMWE) that exhibit both high hydrogen production throughput and exceptional hydrogen purity [18]. However, the anion-exchange membrane (AEM) systems with non-noble

* Correspondence to: Harbin Institute of Technology, School of Materials Science and Engineering , Harbin, China.
E-mail address: jiangsida@hit.edu.cn (S. Jiang).

https://doi.org/10.1016/j.apcatb.2025.126035
Received 3 June 2025; Received in revised form 25 September 2025; Accepted 30 September 2025
Available online 1 October 2025

metals reduce the costs and extend operational lifetimes in alkaline environment, representing an accelerating industrial adoption trend [19]. Achieving high performance and stability at current densities exceeding > 2 A cm^{-2} can significantly enhance production efficiency, reduce costs, and facilitate integration with renewable energy sources [20,21]. Consequently, improving electrocatalyst performance at ultrahigh current densities is critical for advancing AEM electrolyzers.

High-entropy alloys (HEAs) have emerged as an intriguing category of materials owing to their particular properties [22], including the incorporation of multiple elements [23,24], exceptional chemical stability [25,26], enhanced mechanical strength [27,28], and superior catalytic activity [29–31]. These attributes position HEAs as potential electrodes for replacing traditional Ni-based electrodes in industry [32,33]. The "cocktail effect" of HEAs enables the synergistic combination of multiple elements, leading to enhanced catalytic performance [34–36]. Because of the NiFe LDH excellent catalytic performance, most of the researches on HEAs consist of Fe and Ni element [37,38], and Co and Mo are widely recognized for their roles in promoting the surface reconstruction [11,16]. So FeCoNiMo based HEAs have been recently explored and shown excellent oxygen evolution reaction (OER) performance [39–41]. Despite extensive research on HEAs for the oxygen evolution reaction (OER), their further development is hindered by challenges such as complex composition design, difficulty in preparation, and limited stability at high current densities. And it is still challenging to utilize HEAs for AEM industrial applications. To deal with these difficulties, it is essential to further improve performance at high current density by rapid composition screening and heterostructural regulation of HEAs.

As two-dimensional structural defects, grain boundaries could generate localized lattice strain [42], create atomic-level stepped features [43], and provide distinctive catalytic sites for chemical processes [44,45]. Grain boundary segregation engineering (GBSE) is always used to adjust the mechanical properties of alloys [46,47] that leads to directional element doping [48] and local regulation of resistivity [49]. Nowadays, increasing grain boundary density and element segregation via GBSE is proved a direct correlation with enhanced catalytic performance [50,51]. Thus, it is reasonable to assume that GBSE could improve regulate active sites and improve the stability at high current density for OER. The implementation of GBSE depends on the thermodynamic properties of alloy and cooling rate during preparation [52–55]. Compared with magnetron sputtering [56], powder metallurgy [57] and other HEAs prepared methods, melt-extraction [58] features a rapid cooling rate, high production capacity [59], and the ability to control the heterostructure [60–63]. Despite the GBSE has been proved the ability to adjust OER performance, it is still essential to rapidly screen HEA components [64], employ stable preparation methods, and thoroughly investigate the role of grain boundary segregation heterostructure in catalysis.

In this paper, we render a comprehensive theoretical and experimental investigation into the OER activity of HEAs. According to the OER catalytic activity and design rule of GBSE, the components of HEAs are FeCoNiMoCuAl. To streamline component design and prevent overfitting from excessive features, we employ machine learning (ML) techniques to predict the elements ratio of FeCoNiMoCuAl based on the physical properties and conductivity of elements. FeCoNiMoCuAl high-entropy multiphase alloys, screened using ML, were synthesized via an as-cast melt-extracted method, enabling grain boundary segregation of Cu with rapid surface cooling. Structural analysis and density functional theory (DFT) calculations validated the feasibility of regulating catalytic activity by GBSE, showing that grain boundary segregated Cu plays a crucial role in enhancing catalytic performance at high current densities by accelerating electron transfer and improving conductivity. Among the tested samples, $Fe_{20}Co_{20}Ni_{20}Mo_{20}Cu_{15}Al_5$ exhibited the best OER performance, achieving an η of 497 mV at 3 A cm^{-2} and stable operation for 95 h and 40 h at 3 A cm^{-2} and 5 A cm^{-2}. An AEM electrolyzer assembled using $Fe_{20}Co_{20}Ni_{20}Mo_{20}Cu_{15}Al_5$ as both anode and achieved a current density of 0.5 A cm^{-2} at approximately 1.90 V for over 100 h. Additionally, approximately 100 g of HEA fibers were produced in a single preparation at an estimated cost of USD 0.15 per gram, well below that of noble metal catalysts. These findings highlight a novel and efficient approach to designing high-performance industrial catalysts using HEAs, underscoring their potential across various applications.

2. Experimental section

2.1. Machine learning (ML)

Experimental conductivity values of 31 HEAs were collected from the published literature. The collected experimental data covered only single-phase and dual-phase high-entropy alloys, and the machine learning predictions incorporated the influence of high-entropy alloy phase structure. The dataset consists of 26 elements, Sc, Al, Si, Ti, V, Cr, Mn, Fe, Co, Ni, Cu, Zn, Ga, Ge, Zr, Nb, Mo, Rh, Pd, In, Sn, Hf, Ta, W, Ir, and Pt. We used the average and mismatch values (Eqs. (1) and (2)) of 6 elemental properties as input features to avoid the sparsity of the initial composition-set. These elemental properties are conductivity, atomic radius, electronegativity, first ionization energy, first affinity, and covalent radius.

$$\overline{F} = \sum_{i=1}^{n} c_i F_i \tag{1}$$

$$\delta F = \sqrt{\sum_{i=1}^{n} c_i \left(1 - \frac{F_i}{\overline{F}}\right)^2} \tag{2}$$

where $F$and$\overline{F}$ are the average and mismatch values, respectively; c_i and Fi are the content and the corresponding elemental parameter of the *ith* component of a HEA.

The dataset was randomly divided into the training set and the testing set with a ratio of 85 %: 15 %. The input features were scaled to [0, 1] using MinMaxScaler to exclude the influence of the dimensionality of different elemental properties. 7 ML algorithms were introduced to model the conductivity of HEAs, including Multilayer Perceptron (MLP), Random Forest (RF), Bagging, AdaBoosting (Ada), Xgboost (XGB), and Support Vector Machine using polynomials and radial basis functions as kernel functions (SVM_poly and SVM_rbf). The hyperparameters of these algorithms were optimized by an exhaustive algorithm, GridSearch. The prediction accuracy was evaluated by determination coefficient (R^2, Eq. (3)) and root mean square error (RMSE, Eq. (4)). The whole process was completed by Python program.

$$R^2 = 1 - \frac{\sum_{i=1}^{N} (\widehat{y_i} - y_i)^2}{\sum_{i=1}^{N} (y_i - \overline{y})^2} \tag{3}$$

$$RMSE = \sqrt{\frac{1}{N} \sum_{i=1}^{N} (\widehat{y_i} - y_i)^2} \tag{4}$$

where $\widehat{y_i}$ and y_i are the predicted and the experimental target values of the ith sample, respectively, and y is the average value of the target of N samples.

The prediction results of the optimized ML models are showed in Fig. 1b. RF using n_estimators= 96 and max_depth= 4 performs best with the highest R^2 and the lowest RMSE of the training set and the testing set. Fig. 1c exhibits the predicted results by the optimized RF model. The R^2 values higher than 0.85 illustrate the excellent fitting between the predicted conductivity values and the experimental conductivity values. The excellent performance of the optimized RF model on the prediction of new samples is demonstrated by the high predictive accuracy of the testing samples.

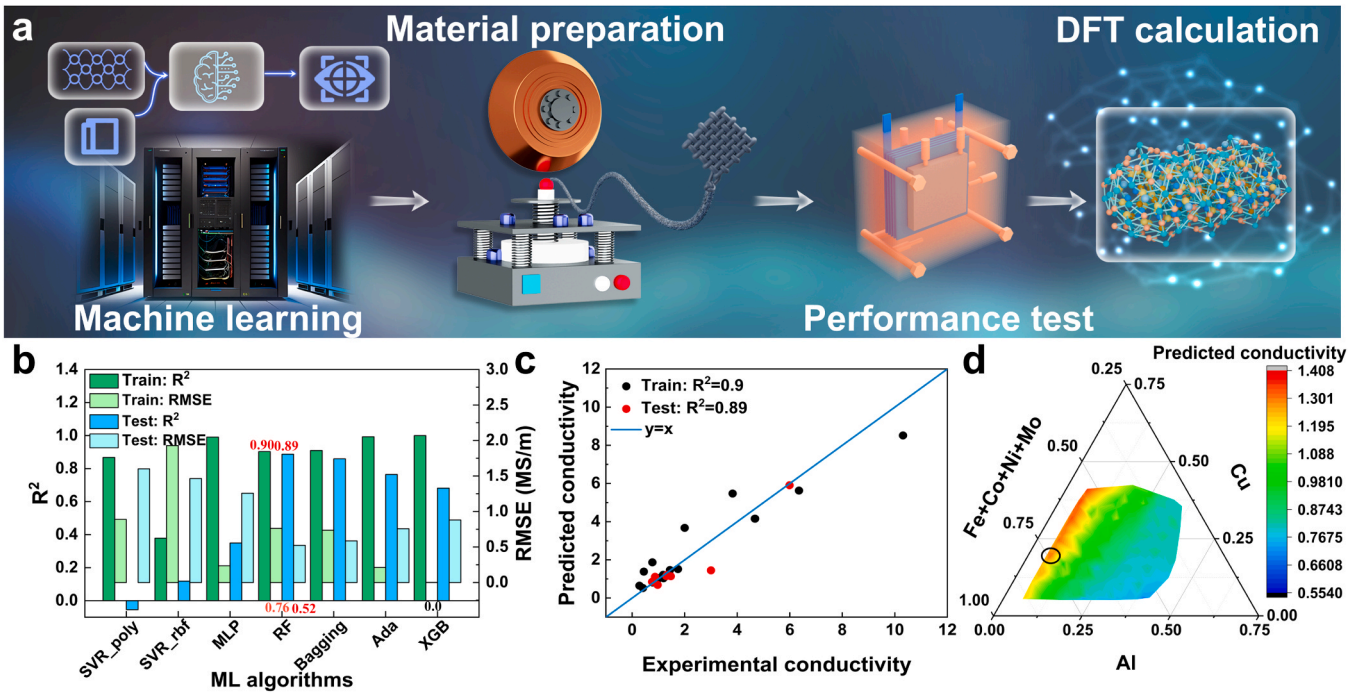

Fig. 1. Rapid screening of OER catalysts for HEAs by machine learning (ML). (a) Design strategy for the electrocatalyst, divided into four steps: ML (Step 1), material preparation (Step 2), performance testing (Step 3), and theoretical calculations (Step 4). (b) Prediction results of optimized ML models showing the RF model performs best with the highest R^2 and lowest RMSE for both the training and testing sets. (c) Conductivity predictions made by the optimized RF model. (d) Predicted conductivity values of various HEAs within the Al-Cu-Fe-Co-Ni-Mo family using the RF model (black circles indicate compositions selected for further testing).

The conductivity values of various HEAs in the $Al_xCu_yFe_zCo_iNi_jMo_k$ family were predicted by the optimized RF model and showed in Fig. 1d. These HEAs follow that 5 at%≤ x, y, z, i, j, and k ≤ 35 at%, and the step size of the compositions is 5 %.

Aimed to design HEAs with perfect activity and stability at high current density, this model predicted only conductivity and had limitations in not predicting phase stability or segregation tendencies. In the future, we will employ the composition-processing-structure-property (CPSP) framework, a two-stage predictive approach that first forecasts crystal structures and subsequently integrates composition and processing data to predict catalytic activity.

2.2. Preparation of HEA fibers

As-cast melt-extracted was used for manufacturing a range of fibers. According to the nominal composition, a total mass of ~120 g of starting materials was mixed using Fe (99.99 %), Co (99.99 %), Ni (99.995 %), Mo (99.99 %), and Al (99.99 %). These elemental powders were provided by the ZhongNuo Advanced Material Technology Co. Ltd., China. Analytical-grade chemical reagents were all utilized immediately, without any additional purification. The beginning materials were smelted 4–5 times using vacuum arc smelting to guarantee that the components are evenly combined while being shielded by high-purity argon (99.999 %). Then, the metal rod (about 2–3 cm) was melted in a high-purity BN crucible, and the resulting solution was dipped in oxygen and discarded as soon as the copper wheel began to rotate and met the molten surface. Ultimately, HEA fibers measuring around 3–4 cm in length, 30–35 μm in diameter and ~115 g in total mass were produced. Among all the elements, aluminum corrodes the easiest. To increase the specific surface area, porous morphological characteristics were realized via a typical dealloying corrosion strategy in 1.0 M HCl. After dealloying, the as-obtained fibers were successively cleaned by absolute ethyl alcohol (99.5 %) and distilled water (18.2 MΩ•cm) for 30 min.

2.3. Physical characterization

The morphology of fibers was characterized by field-emission scanning electron microscopy (FE-SEM) and transmission electron microscopy (TEM). Scanning electron microscopy (SEM) observations were made using the Carl Zeiss Merlin Compact and TEM analysis was conducted using an FEI Talos F200s, operating at 200 kV. The Electron Back Scatter Diffraction (EBSD) was carried out using a Oxford Symmetry2. Crystallographic information was obtained using Maivern Panalytical Empyrean X-ray diffractometer, equipped with Cu Kα radiations (λ= 1.5418 Å). Raman spectra were collected using a LabRAM HR Evolution. X-ray photoelectron spectroscopy (XPS) was carried out using a ThermoFisher Scientific Esca Xi+, equipped with Al Kα radiations (1486.6 eV). Brunner-Emmet-Tellmeasurement (BET) measurements on a Micromeritics ASAP 2460 at 77 K. The inductively-coupled plasma-optical emission spectrometry (ICP-OES) was measured using Thermo iCAP 740.

2.4. Electrochemical Measurements

Electrochemical measurements were conducted using an electrochemical working station (CHI 760E) in a three-electrode setup, where 1 M KOH solution was used as an electrolyte, an Hg/HgO electrode (in 1 M KOH) was used as a reference electrode and the graphite rod (99.9 %, with a diameter of 8 mm) was used as a counter electrode. Oxygen evolution reaction (OER) overpotential (η) was calculated using the following relationship:

$$E(RHE) = E(Hg/HgO) + 0.059pH + 0.098 \quad (5)$$

LSV and Tafel curves were corrected by 95 % iR compensation for the ohmic loss except for AEM test. Electrochemical impedance spectroscopy (EIS) was carried out at 1.58 V in the frequency range of 1000 kHz to 10 mHz with an amplitude of 5 mV. EIS analysis was carried out by fitting the Nyquist plot using an equivalent circuit, which was realized by the Z-view software. Chronopotentiometry

measurements were performed to evaluate the long-term stability. The electrochemical surface area (ECSA) was determined by measuring the capacitive current associated with double-layer charging from five different scan-rates (10, 30, 50, 70, 90 and 110 mV s^{-1}). In these regions, the integrated charge should be due to the charging of the electrode-electrolyte double layer. The double-layer charging current (i), normalized on the geometric area of the electrode, is directly proportional to the scan rate (υ), i.e., $i = \upsilon C_{dl}$. By drawing the curves of anodic and cathodic currents with respect to the scan rate, the average C_{dl} of linear fitting slope is derived. The measured capacitance currents are plotted as a function of the scan rate, as shown in Fig. S16. According to the reported typical value, the specific capacitance (C_s) of electrocatalyst in 1 M KOH is selected as $C_s = 0.040$ mF cm^2. Therefore, the ECSA of the catalyst layer can be calculated using Eq. (6).

$$ECSA = C_{dl}/ C_s \quad (6)$$

About 10 HEA-Cu4 fibers were arranged in parallel function and employed as catalyst materials for the anode and cathode in AEM. The active area corresponds to the collective geometric surface area of the fibers (assumed as cylinder). The Electric conduction and electrolyte transport are performed by S-type Ti current collectors with a serpentine flow field. The AEM electrolyser was put together with the cathode or anode compartment first, followed by the end plate, sealing gasket, Ti current collector, DE 4 h HEA fibers, and sealing gasket. An anion-exchange membrane (Fumasep FAA-3-PK-130) was employed to divide the electrolyser's cathode and anode compartments. A peristaltic pump was used to regulate the flow of 1.0 M KOH electrolyte to both sides of the electrolyser at a rate of 2.5 ML min^{-1} throughout the testing.

2.5. Theoretical calculations

All density functional theory calculations were performed by Vienna ab initio simulation package (VASP) [65]. The Perdew-Burke-Ernzerhof (PBE) [66] functional was employed to treat the exchange-correlation interactions. The plane-wave basis set with a kinetic energy cutoff of 400 eV, the energy convergence criterion of 10^{-4} eV, the force convergence criterion of 0.02 eV $Å^{-1}$, and a (1 ×1 ×1) Monkhorst-Pack k-point sampling was employed for structure relaxation. A sufficiently large vacuum gap (> 12 Å) was employed to prevent the interaction between neighboring periodic structures. H_2 and H_2O were calculated in boxes of 20 Å× 20 Å× 20 Å with the gamma point only. The free energy diagrams for OER were calculated with reference to the computational hydrogen electrode followed the work of Nørskov et al. [67] Under the standard reaction condition, the chemical potential of a proton and electron pair ($\mu(H^+ + e^-)$) is equal to a half of gaseous hydrogen ($\mu(H_2)$). The free energy of gas phase and adsorbed species can be obtained from the following equation:

$$\Delta G = \Delta E_{DFT} + \Delta ZPE - T\Delta S + G_U \quad (7)$$

where T was set as 298.15 K. ΔZPE and TΔS was the change in the zero-point energy and entropy. ΔE_{DFT} is the total energy calculated by VASP. G_U is the influence of electrode potential.

$$G_U = -neU \quad (8)$$

3. Results and discussion

3.1. HEAs design strategy based on ML and GBSE

The complex composition of HEAs provides immense potential for developing electrocatalysts with outstanding performance. Selective HEA design is therefore essential to efficiently synthesize electrocatalysts with desired characteristics [68]. We propose a four-step approach that integrates theoretical and experimental methodologies for HEA electrocatalyst design (Fig. 1a). Recently, ML has emerged as a powerful tool for extracting information and predicting performance based on material composition [69–71]. The selection of the six elements (Fe, Co, Ni, Mo, Cu, and Al) for this study was guided by the principles of GBSE and the cocktail effect. Fe and Ni serve as active sites for the OER process, while Co and Mo accelerate surface reconstruction. Al can be selectively removed through dealloying to increase surface area, and Cu could increase conductivity and adjust heterostructures via GBSE. To predict the elements ratio of FeCoNiMoCuAl with high conductivity and prevent overfitting from excessive features, namely conductivity, atomic radius, electronegativity, first ionization energy, electron affinity, and covalent radius, were incorporated into the dataset. The dataset was randomly divided into training (85 %) and testing (15 %) subsets, and input features were normalized to [0, 1] using MinMaxScaler to minimize the impact of dimensional variability among elemental properties. The selection of an optimal modeling and testing algorithm is a critical step before constructing the ML model. The prediction results of the optimized ML models are illustrated in Fig. 1b. Among these, the RF algorithm with n_estimators = 96 and max_depth = 4 exhibited the best performance with the highest R^2 value and lowest RMSE for both the training and testing datasets, indicating further reduces model complexity and mitigates overfitting risks compared to the default parameters of 100 and None. The R^2 values exceeding 0.85 indicate a strong correlation between the predicted and experimental conductivity values, confirming the high accuracy of the optimized RF model. The dataset was randomly divided 1000 times into training and testing part to further evaluate the generalization performance of the established RF model. The mean accuracy of the testing set is 0.87, demonstrating the excellent generalization capacity of the established RF model. In addition, Fig. S1 shows the excellent agreement between the experimental conductivity values and those predicted by the model. The corresponding predictions from the optimized RF model are displayed in Fig. 1c. To achieve high performance and stability under ultra-high current densities, HEA catalysts must feature several active sites and maximize conductivity. Based on the predictions of the RF model, the composition range within the black circle in Fig. 1d, approximately $(FeCoNiMo)Cu_{15–25}Al_{0–25}$, was identified as optimal.

Based on the ML results, four HEA compositions, namely $Fe_{20}Co_{20}Ni_{20}Mo_{20}Cu_{20}$ (HEA-Cu1), $Fe_{20}Co_{20}Ni_{20}Cu_{20}Al_{20}$ (HEA-Cu2), $Fe_{20}Co_{20}Ni_{20}Mo_{20}Cu_5Al_{15}$ (HEA-Cu3), and $Fe_{20}Co_{20}Ni_{20}Mo_{20}Cu_{15}Al_5$ (HEA-Cu4), were selected to investigate the optimal Cu and Al ratios and the effects of Mo and Al on catalytic performance. These HEA samples were synthesized using a melt-extraction process, ensuring both faster cooling rate and precise control over composition. Under a higher degree of supercooling, the weakening of atomic diffusion leads to the tendency to form small grains and produce various defects, that would induce grain boundary segregation [60]. The actual composition closely matched the nominal composition of $Fe_{20}Co_{20}Ni_{20}Mo_{20}Cu_{15}Al_5$ (Table S1), confirming the accuracy of the preparation method. Scanning electron microscopy (SEM) indicated the fibers had diameters of approximately 30 μm with smooth surface morphologies (Fig. 2a). To enhance the specific surface area, dealloying was applied to remove Al, resulting in a porous fiber surface structure (Fig. 2a inset and Fig. S2). To identify the best duration of dealloying, the LSV curves of each HEA samples were tested. The optimal dealloying durations for HEA-Cu1, HEA-Cu2, HEA-Cu3, and HEA-Cu4 are 4 h, 3 h, 4 h, and 4 h, respectively. (Fig. S3). For HEA-Cu4, the quantity and volume of the pore increased under 1 h to 4 h (Fig. S4). After 5 h dealloying, extensive surface exfoliation occurs on the fibers, resulting in loss of cylindrical integrity and manifesting as a pronounced increase in brittleness (Fig. S5). Furthermore, among the samples after best dealloying durations, HEA-Cu4 exhibited the largest specific surface area (Table S2) and was selected for further microstructural analysis.

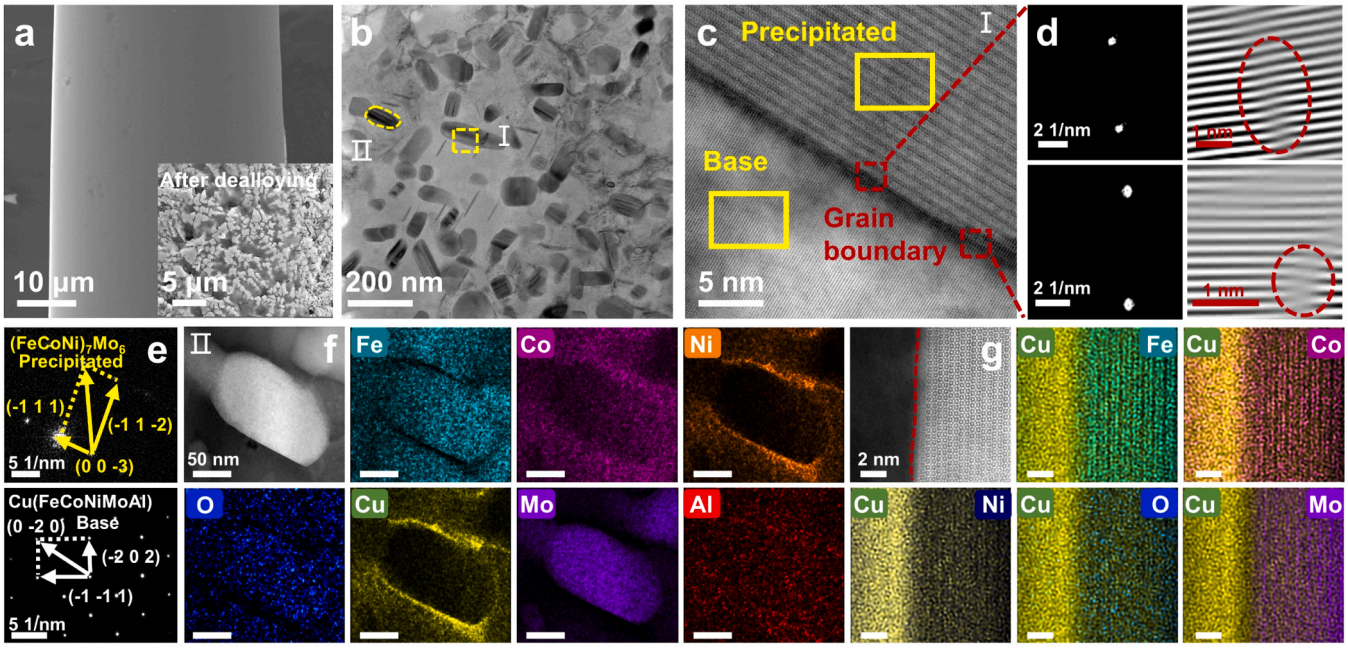

Fig. 2. Structural characterization of HEA-Cu4 that guided by GBSE. (a) SEM image of as-prepared fibers (the inset displays the surface of fiber after dealloying). (b) TEM image of HEA-Cu4 revealing two distinct crystalline phases. (c) HRTEM image of the boundary between the two phases, with white and yellow dashed squares highlighting the SAED images of the base phase and precipitated phase, respectively. (d) FFT and IFFT images of the red square frame region in c. (e) FFT image of base phase and precipitated phase. (f) EDS analysis of the boundary between the two phases. (g) Elements mapping results illustrating atomic distribution across the boundary.

3.2. Structure characterization of grain boundary segregation

X-ray diffraction (XRD) patterns (Fig. S6) revealed a well-defined crystalline structure. Specific phases identified included $Al_{0.9}Ni_{1.1}$ (ICDD-PDF-2, card no: 44–1185) in HEA-Cu2 and Cu (ICDD-PDF-2, PDF card no: 85–1326) along with Co_7Mo_6 (ICDD-PDF-2, PDF card no: 29–0489) in HEA-Cu1, HEA-Cu3, and HEA-Cu4. These results demonstrated the atomic proportion of Cu could influence the phase structure. A cross-sectional transmission electron microscopy (TEM) picture was acquired using a focus-ion beam (FIB) technique (Fig. S7) revealed two distinct crystalline phases (Fig. 2b). The selected area electron diffraction (SAED) pattern (Fig. 2e) corresponded to a face-centered cubic Cu (FeCoNiMoAl) crystal and a hexagonal close-packed $(FeCoNi)_7Mo_6$ crystal, exhibiting a non-uniform elemental distribution (Fig. S8). The quantitative phase analysis was achieved by using Electron Back Scatter Diffraction (EBSD). The results demonstrated that the volume fraction of base phase is significantly larger than nano-sized precipitated phase (Fig. S9). Within localized regions, a large number of nano-sized precipitated phases increased the grain boundaries density which will benefit for OER [50,72]. Stable crystalline base phase provided active sites and self-supporting ability for OER. Line-scan results (Fig. S10) and energy-dispersive X-ray spectrometry (EDS) maps (Fig. S11) demonstrated a significant decrease in Cu distribution transitioning from the base phase to the precipitated phase. The Al element showed instability due to dealloying. The Cu element concentrated at the boundary between the two phases, aligning with the goal of using GBSE to regulate the heterostructure (Fig. 2f), that was attributed to the negative mixing enthalpy between Cu and other elements, particularly Ni, and insufficient diffusion under high undercooling. (Table S3) [60,73]. Furthermore, farther atomic-level mapping (Fig. 2g) confirmed the distribution of Fe, Co, Ni, Mo, O, and Cu in the precipitated phase, with Cu and Ni accumulating at the grain boundary. The grain boundary in Fig. 2c presented severe lattice distortion and dislocation defects, which was also identified by the lattice fringes in the inverse fast Fourier transform (IFFT) images (Fig. 2d). As defects often function as active and selective sites, they therefore boost the activity of Ni sites at the grain boundaries. At the same time, the segregation of Cu with high conductivity at grain boundaries could change the grain boundary charge and assume the role of load transfer. These results confirmed Cu-induced boundary segregation via GBSE, facilitating the restructuring of active sites at the phase interfaces and constructing network to enhance the conductivity of the catalyst.

The surface chemical states of the samples after dealloying were analyzed using X-ray photoelectron spectroscopy (XPS). The Cu 2p spectra (Fig. S12a) revealed a $2p_{1/2}$ binding energy of 932.4 eV, corresponding to Cu^0. Dealloying induced the oxidation of Fe, Co, Ni, and Mo from their metallic states (Fe^0, Co^0, Ni^0, Mo^0) to higher valence states (Fig. 3a and Fig. S12b-d). The Al^0 fully transformed into Al^{2+} and Al^{3+} in HEA-Cu4, signifying effective dealloying, corroborated by SEM images (Fig. S12e). Furthermore, HEA-Cu4 exhibited the highest levels of Ni^{3+} and M-OOH among the four samples, indicating a greater number of active sites [74] to enhance the OER process (Fig. 3a-b). Ultraviolet photoelectron spectroscopy (UPS) data were used to examine d-band center fluctuations. All samples had work functions around 5 eV (Fig. S12f). The *d*-band center of HEA-Cu4 was closer to the Fermi level (E_F) compared to HEA-Cu1 (~0.68 eV), HEA-Cu2 (~0.61 eV), and HEA-Cu3 (~0.39 eV) (Fig. 3c), indicating superior adsorption capacity [75]. In general, XPS and UPS analyses verified that $Fe_{20}Co_{20}Ni_{20}Mo_{20}Cu_{15}Al_5$ exhibited the highest number of active sites and superior adsorption capacity, likely contributing to its enhanced catalytic performance.

3.3. Electrocatalytic OER and HER performances

The electrochemical OER activity of different electrodes was evaluated in 1 M KOH. The linear sweep voltammetry (LSV) curves (Fig. 3d) showed that HEA-Cu4 delivered the best catalytic performance, with overpotentials (η_{10}) of 238 mV and (η_{3000}) of 497 mV. To ensure the performance of the fibers, the LSV curves of the fibers were tested repeatedly (Fig. S13a). The measured overpotentials exhibited minimal deviation from reported values, with differences of ~6.6 mV at 10 mA cm^{-2} and ~8 mV at 0.2 A cm^{-2}. (Fig. S13b). In contrast, HEA-

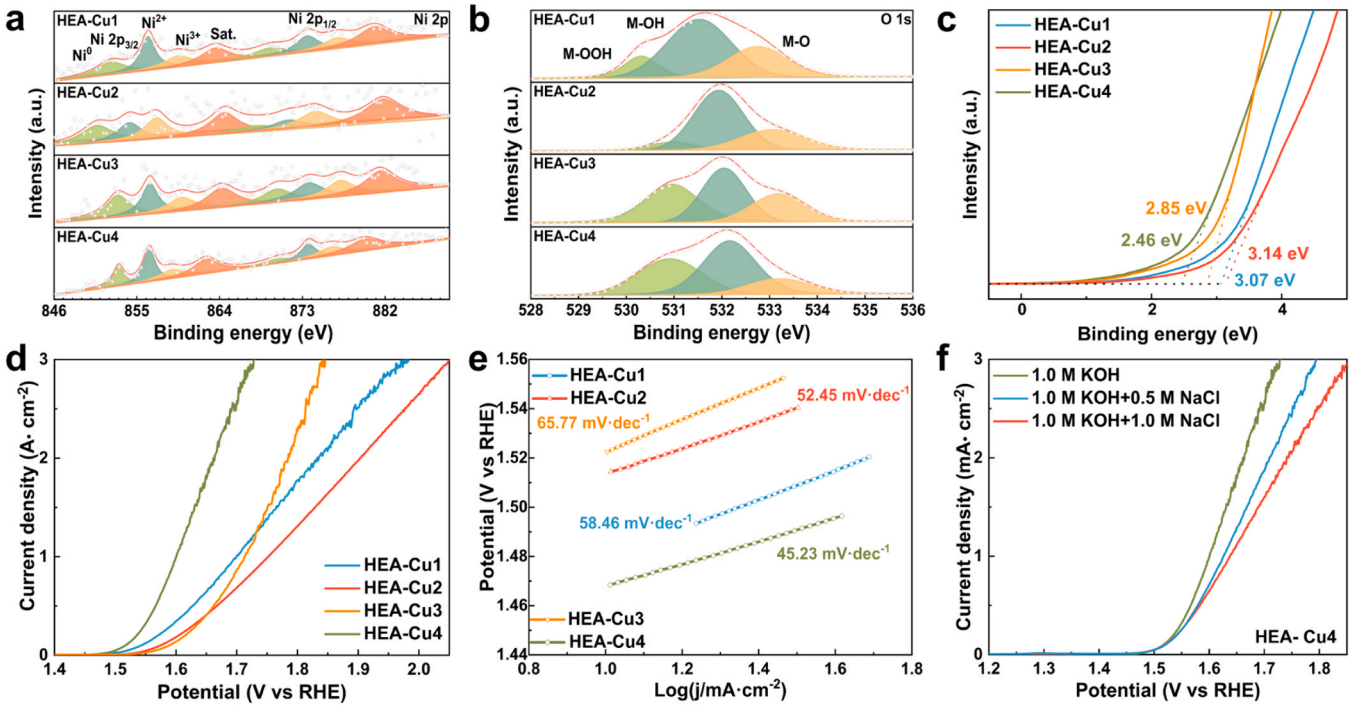

Fig. 3. Photoelectron energy spectra and electrochemical OER performance in acidic medium of HEAs samples. (a) Ni 2p XPS spectra. (b) O 1 s XPS spectra. (c) Valence band position and work function distance. (d) LSV curves for four high-entropy alloy samples (iR corrected, scan rate: 5 mV s^{-1}) in 1.0 M KOH. (e) Tafel plots derived from the data in d. (f) LSV curves of various samples (iR corrected, scan rate: 5 mV s^{-1}) in 1.0 M KOH with differing NaCl concentrations.

Cu1, HEA-Cu2, and HEA-Cu3 exhibited significantly higher η_{3000} values of 750, 820, and 612 mV, respectively. HEA-Cu4 also demonstrated the smallest Tafel slope (45.23 mV dec^{-1}), indicating faster OER kinetics [16] compared to HEA-Cu1 (58.46 mV dec^{-1}), HEA-Cu2 (52.45 mV dec^{-1}), and HEA-Cu3 (65.77 mV dec^{-1}) (Fig. 3e). These results establish HEA-Cu4 as one of the most efficient HEA-based OER electrocatalysts at high current densities (Table S4 and Fig. S15). Electrochemical impedance spectroscopy (EIS) rendered Nyquist plots fitted to a Randles circuit (Fig. S14a). HEA-Cu4 exhibited the lowest charge transfer resistance (R_{ct} ~70.5 Ω), which was significantly lower than that of HEA-Cu1 (~192.8 Ω), HEA-Cu2 (~289.6 Ω), and HEA-Cu3 (~71.5 Ω), indicating faster Faradic processes. The electrochemical surface area (ECSA), estimated using the double-layer capacitance (C_{dl}) obtained from cyclic voltammetry (CV) (Fig. S16), showed that HEA-Cu4 had the highest C_{dl} value (2.020 mF cm^{-2}) compared to HEA-Cu1 (0.087 mF cm^{-2}), HEA-Cu2 (0.922 mF cm^{-2}), HEA-Cu3 (0.261 mF cm^{-2}) (Fig. S17). This indicates

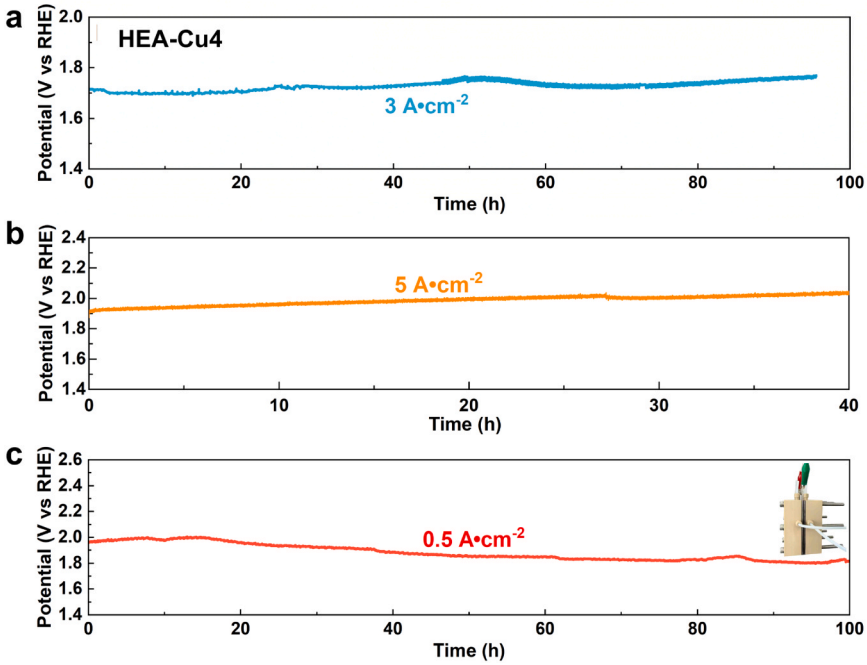

Fig. 4. Electrochemical stability of HEA-Cu4. (a-b) Chronopotentiometry curves of HEA-Cu4 at industrial-grade current densities of 3 and 5 A cm^{-2}. (c) Chronopotentiometry curve of the AEM electrolyser at a current density of 0.5 A cm^{-2} without iR correction (the inset displays the actual AEM electrolyser).

that HEA-Cu4 had the highest exposure of active sites. For the HER, HEA-Cu1, HEA-Cu2, HEA-Cu3, and HEA-Cu4 achieved overpotentials of 420, 595, 523, and 289 mV, respectively, at a current density of 0.2 A cm^{-2} (Fig. S18a). Tafel slopes and R_{ct} values further confirmed the superior HER kinetics and electron transfer ability of HEA-Cu4 (Fig. S18b-d). The excellent OER and HER performance of HEA-Cu4 demonstrated that it had the ability to be used as both the anode and cathode for water splitting. To address practical industrial applications in challenging environments, HEA-Cu4 electrodes were tested in low temperatures and simulated seawater electrolytes. The electrodes exhibited excellent performance in simulated seawater (1.0 M KOH+0.5 M NaCl) electrolytes and at 10 ℃, achieving η_{3000} of 526 and 610 mV, respectively (Fig. 3f and Fig. S14b), enhancing their application potential.

Electrochemical stability under industrial-scale conditions was evaluated at ultrahigh current densities. The chronopotentiometry (CP) curves of HEA-Cu4 fiber maintained stability for 800, 320, and 95 h at current densities of 1, 2, and 3 A cm^{-2}, respectively (Fig. 4a and Fig. S19a-b) and notably, as shown in Fig. 4b, HEA-Cu4 exhibited excellent catalytic stability at current density of 5 A cm^{-2}, with only slight degradation after 40 h. The LSV curves before and after 95 h stability test at 3 A cm^{-2} showed a promotion in OER activity under 0.2 A cm^{-2}, however the overpotential increased by ~15 mV at 3 A cm^{-2} (Fig. S22). Long-term chronoamperometry (CA) tests were conducted to evaluate the stability of the HEA-Cu4 catalyst at constant potentials corresponding to current densities of 3 and 5 A cm^{-2} for 95 and 40 h, respectively (Fig. S20). The catalyst demonstrated exceptional stability at 3 A cm^{-2} over 95 h. In contrast, at the higher current density of 5 A cm^{-2}, a modest current decay of 17.5 % was observed over 40 h. In conclusion, HEA-Cu4 demonstrates superior OER stability under high current densities compared to most reported catalysts (Table S4). For HER, HEA-Cu4 exhibited excellent catalytic stability at 1 A cm^{-2}, with slight degradation approaching 380 h (Fig. S21). Additionally, an anion-exchange membrane (AEM) electrolyzer was assembled employing HEA-Cu4 as both the anode and cathode (Fig. 4c). Notably, the AEM electrolyzer achieved a current density of 0.5 A cm^{-2} with reduced voltage and demonstrated stable operation for approximately 100 h. These outstanding stability performances underline the significant potential of this material for industrial applications (Table S6). After long-time stability tests, SEM analysis confirmed that the fiber retained its self-supporting structure. While Al was almost entirely removed after dealloying, other elements showed minimal loss during the tests (Fig. S23). Furthermore, the HEA-Cu4 still maintained base phase and precipitated phase heterostructure (Fig. S24a), and the Cu and Ni concentrated at the boundary between the two phases (Fig. S24b). Excellent OER performance and heterostructure stability at high current density lighted the possibility of industrial applications. Following the stability test, the distribution of Co and Ni in the precipitated phase became more pronounced relative to the initial heterostructure (Fig. 2f), at the same time, the initially disordered Cu solid solution became internally homogenized (Fig. S8). This electrochemical reconstruction of precipitated base during catalysis may contribute to the observed activity degradation.

3.4. Mechanism investigation for OER process

The catalytic reaction pathway was further investigated by introducing methanol into the electrolyte (Fig. S14c). The results indicated that HEA-Cu4 exhibited moderate adsorption of oxygen-containing intermediates, which facilitated the catalytic reaction [76]. The four samples' surface elements changes were investigated using in situ Raman spectroscopy. As the applied voltage increased, two distinct peaks emerged at approximately 472 and 554 cm^{-1} (Fig. S25), corresponding to the E_g bending vibrations (δ(Ni-O)) and $A_{1\,g}$ stretching vibrations (ν(Ni-O)) in NiOOH. Among four samples, HEA-Cu4 exhibited the earliest emergence of the Ni^{3+} Raman peak, which indicates a faster surface reconstruction process during the OER and clarify the grain boundaries promote the OER process [77,78]. Compared with other samples, HEA-Cu2 displayed no peaks even at 1.40 V, indicating that the addition of Mo would accelerate the transformation to active Ni^{3+} species. The peak area of NiOOH of HEA-Cu3 and HEA-Cu4 furtherly demonstrated that the activity of Ni sites was promoted by Cu. Raman spectroscopy was conducted to identify changes in surface active species before and after stability (Fig. S26). After stability test, the peaks strength enhanced at around 150, 281, 472, 554 and 715 cm^{-1}, which belonged to FeOOH [79] and NiOOH that is always regarded as active substance for OER [80], indicating M-OOH serves as an active species during the reaction, in agreement with XPS results. Moreover, peaks were observed at approximately 472 and 554 cm^{-1}, which can be assigned to the E_g bending (δ(Ni-O)) and $A_{1\,g}$ stretching (ν(Ni-O)) vibrations of NiOOH, respectively. The calculated intensity ratio ($I_δ/I_ν$) of about 4.1 suggests the transformation of Ni species into high-valence γ-NiOOH during the OER, a state which is beneficial for catalytic activity.

The catalytic mechanism of the grain boundary segregation heterostructure was further examined using DFT simulations. Previous studies [81,82] have identified Ni and Co sites as primary active species in the catalytic process; however, Cu is often considered secondary. To elucidate the role of Cu at the grain boundary during the OER, models of the base phase and precipitated phase were constructed based on TEM results, along with models without Cu (Fig. 5a). According to adsorbed reaction intermediate changes of base phase (Figs. S27 and S28) and precipitate phase (Fig. S29) for OER process, the Gibbs free energy changes (ΔG) were calculated for different models at 0, 1.23, and 1.8 V using the $4e^-$ pathway mechanism to evaluate OER energy barriers. For the base phase, the rate-determining step (RDS) on Ni and Co sites at 0 V was the oxidation of *OOH to O_2, with ΔG_{max} values of 5.999 and 6.846 eV, respectively. Conversely, Fe, Mo and Cu sites exhibited lower ΔG_{max} values of 4.430, 2.958 and 1.827 eV, respectively, with their RDS being the oxidation of *O to *OOH (Fig. S30a). Based on the ΔG_{max} values, the Cu sites are identified as the preferential active sites for the OER. As the voltage increased, the ΔG_{max} for Fe, Ni, Co, and Mo sites changed from 2.200, 4.770, 5.036, and 1.728 eV at 1.23 V (Fig. S30b) to 2.620, 4.190, 5.616, and 1.158 eV at 1.8 V, respectively (Fig. 5b). Notably, the Cu site demonstrated the most favorable catalytic activity at high voltage, with the lowest ΔG_{max} of 0.027 eV at 1.8 V (Fig. 5c). Ni, Mo, and Cu sites exhibit enhanced activity with increasing voltage, while Co sites activity decreased. The ultralow energy barrier at Cu sites under 1.8 V potential likely constitutes the primary reason for superior activity of HEA-Cu4 at high current densities. Elements exhibiting higher catalytic activity, such as Fe, Co, and Ni, typically demonstrate stronger adsorption capabilities. Partial density of states (pDOS) analysis confirmed that Cu sites effectively modulate the adsorption capacity of HEA-Cu4, shifting the d-band center away from the Fermi level and thereby facilitating the desorption step in catalytic reactions. (Fig. 5d) [83]. In the precipitated phase, Ni sites displayed a lower ΔG_{max} of 1.81 eV (Fig. 5e) at 0 V compared to Cu sites at 3.220 eV (Fig. S30d).

When comparing the HEA-Cu4 and $Fe_{23}Co_{23}Ni_{23}Mo_{23}Al_8$ phase models, HEA-Cu4 exhibited lower ΔG_{max} value of Ni sites in both the primary phase (5.999, 4.770, and 4.190 eV at 0, 1.23, and 1.8 V) (Fig. S30c) and precipitated phase (1.81 and 0.58 eV at 0 and 1.23 V), (Fig. 5f) indicating the Cu sites improved the activity of Ni sites. Differential charge and Bader charge analyses (Fig. 5a) showed that at the grain boundary, about 0.17 and 0.25 electrons were transferred of $Fe_{23}Co_{23}Ni_{23}Mo_{23}Al_8$ and HEA-Cu4, respectively, suggesting that the co-segregation of Cu and Ni at grain boundaries promotes electron transfer and benefits to the OER process. For different calculated sites, the volcano plot relationship between - η^{OER} and the value of ΔG_{*O}-ΔG_{*OH} were analyzed to compared the activity (Fig. S31). Compared with $Fe_{23}Co_{23}Ni_{23}Mo_{23}Al_8$, the Cu sites at base phase and Ni sites at precipitated phase of HEA-Cu4 displayed at the top of the volcano plot, indicating the addition of Cu promoted the activity for OER. DFT

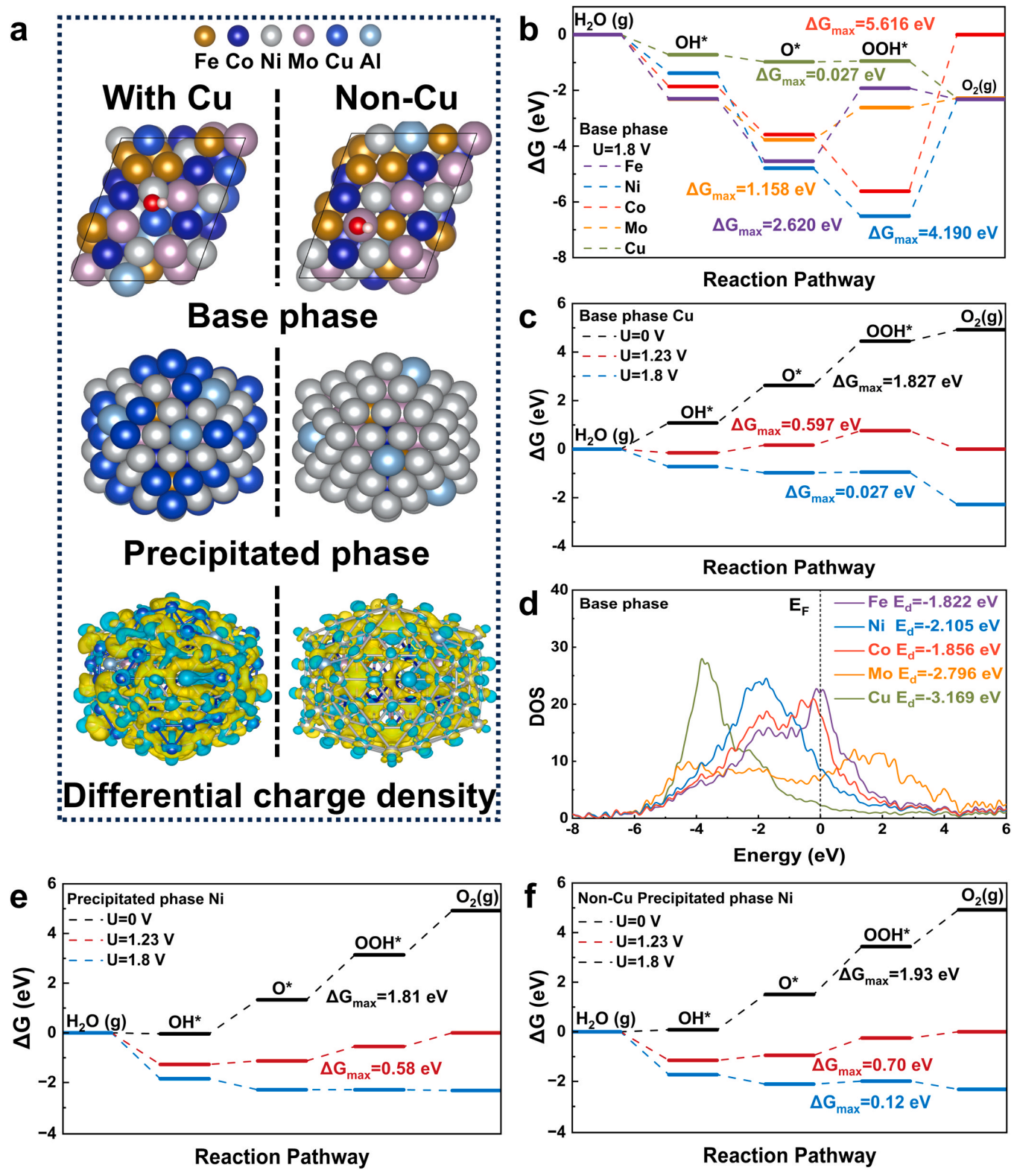

Fig. 5. DFT calculations for the structural configuration and energetic reaction pathways. (a) Calculation models of the base and precipitated phases for HEA-Cu4 and $Fe_{23}Co_{23}Ni_{23}Mo_{23}Al_8$, along with corresponding differential charge density results for the precipitated phase (yellow and blue areas inducate charge accumulation and depletion, respectively). (b) Gibbs free energy changes for four step in the OER process at at Fe, Ni, Co, Mo, and Cu sites in the base phase at 1.8 V. (c) Gibbs free energy changes for OER reaction steps at Cu sites in the base phase at 0, 1.23, and 1.8 V. (d) Partial density of states (pDOS) for Fe, Co, Ni, Mo, and Cu in the base phase. (e-f) Gibbs free energy changes for OER reaction steps at Ni sites in the precipitated phases of HEA-Cu4 and $Fe_{23}Co_{23}Ni_{23}Mo_{23}Al_8$ at 0, 1.23, and 1.8 V.

calculation results demonstrated that the Cu site exhibits superior catalytic activity at high voltage and enhances the activity of Ni sites by decreasing ΔG_{max} and promoting electron transfer of the grain boundary. At the same time, these results further confirmed the beneficial effect of grain boundary segregation heterostructure on site catalytic activity.

4. Conclusion

In this paper, we present an efficient strategy for designing an HEA-based electrocatalyst by integrating machine learning, material synthesis, performance evaluation, and theoretical calculations. The grain boundary segregation high-entropy multiphase alloy electrocatalyst achieved exceptional catalytic performance, demonstrating stability at 5 A cm^{-2} for the OER, surpassing or matching the performance of previously reported electrocatalysts. Additionally, the $Fe_{20}Co_{20}Ni_{20}Mo_{20}Cu_{15}Al_5$ catalyst exhibited outstanding overall water-splitting performance as both anode and cathode in an AEM electrolyzer. These findings highlight the grain boundary segregation engineering is an effective directional doping method. The high-entropy base phase provides catalytic active sites, while the nano-sized precipitated phase increased the density of grain boundary. The segregated Cu element locally at the grain boundary of the precipitate phase promotes the electrons transfer and improves the catalytic activity of active sites at high current densities. Nevertheless, challenges remain in scaling up HEA fibers to fabricate large electrocatalysts suitable for industry electrolyzers. Despite this, the effective design process, together with outstanding catalytic performance and lower costs than noble metals, highlight the considerable industrial potential of HEA-based catalysts.

CRediT authorship contribution statement

Bo Li: Methodology, Investigation, Data curation. **Yonghui Wang:** Formal analysis. **gang Wang:** Methodology. **Yu Sui:** Writing – review & editing. **Jianhua Li:** Writing – review & editing. **Juntao Huo:** Writing – review & editing, Methodology. **Yan Du:** Formal analysis. **Jiaqi Huang:** Formal analysis, Data curation. **Zhenwen Yu:** Formal analysis, Data curation. **Sida Jiang:** Writing – review & editing, Methodology, Funding acquisition, Conceptualization. **Yifan Cui:** Writing – original draft, Visualization, Validation, Supervision, Software, Resources, Project administration, Methodology, Investigation, Funding acquisition, Formal analysis, Data curation, Conceptualization. **Jianfei Sun:** Writing – review & editing, Methodology.

Declaration of Competing Interest

The authors declare that they have no known competing financial interests or personal relationships that could have appeared to influence the work reported in this paper

Acknowledgements

This work was supported by the National Natural Science Foundation of China (Grant Nos. 52271028), the Aeronautical Science Foundation of China(2024Z063077001), the Science and Technology Innovation Talent Project of Harbin(2023CXRCGD029), the Key Research and Development Plan of Heilongjiang Province(2024ZX02C24), and the Fundamental Research Funds for the Central Universities (HIT. DIJJ.2023166).

Appendix A. Supporting information

Supplementary data associated with this article can be found in the online version at doi:10.1016/j.apcatb.2025.126035.

Data availability

No data was used for the research described in the article.

References

[1] Q. Fu, L.W. Wong, F. Zheng, X. Zheng, C.S. Tsang, K.H. Lai, W. Shen, T.H. Ly, Q. Deng, J. Zhao, Unraveling and leveraging in situ surface amorphization for enhanced hydrogen evolution reaction in alkaline media, Nat. Commun. 14 (2023) 6462.
[2] F. Lyu, S. Zeng, Z. Jia, F.-X. Ma, L. Sun, L. Cheng, J. Pan, Y. Bao, Z. Mao, Y. Bu, Y. Y. Li, J. Lu, Two-dimensional mineral hydrogel-derived single atoms-anchored heterostructures for ultrastable hydrogen evolution, Nat. Commun. 13 (2022) 6249.
[3] H. Liu, R. Xie, Y. Luo, Z. Cui, Q. Yu, Z. Gao, Z. Zhang, F. Yang, X. Kang, S. Ge, S. Li, X. Gao, G. Chai, L. Liu, B. Liu, Dual interfacial engineering of a chevrel phase electrode material for stable hydrogen evolution at 2500 mA cm−2, Nat. Commun. 13 (2022) 6382.
[4] H. Zhang, K. Song, Z. Lin, Z. Wang, L. Zhang, S. Shen, L. Gu, W. Zhong, In situ reconstructed ru clusters on $LaRuSi_3$ with enhanced electrocatalytic activity for alkaline hydrogen evolution, Adv. Funct. Mater. 34 (2024) 2405897.
[5] Q. Shi, C. Zhu, D. Du, Y. Lin, Robust noble metal-based electrocatalysts for oxygen evolution reaction, Chem. Soc. Rev. 48 (2019) 3181–3192.
[6] S. Liu, W.H. Huang, S. Meng, K. Jiang, J. Han, Q. Zhang, Z. Hu, C.W. Pao, H. Geng, X. Huang, C. Zhan, Q. Yun, Y. Xu, X. Huang, 3D Noble-Metal nanostructures approaching atomic efficiency and atomic density limits, Adv. Mater. 36 (2024) 2312140.
[7] Z. Wang, Z. Lin, Y. Wang, S. Shen, Q. Zhang, J. Wang, W. Zhong, Nontrivial topological surface states in Ru_3Sn_7 toward wide pH-range hydrogen evolution reaction, Adv. Mater. 35 (2023) 2302007.
[8] K. Song, H. Zhang, Z. Lin, Z. Wang, L. Zhang, X. Shi, S. Shen, S. Chen, W. Zhong, Interfacial engineering of cobalt thiophosphate with strain effect and modulated electron structure for boosting electrocatalytic hydrogen evolution reaction, Adv. Funct. Mater. 34 (2024) 2312672.
[9] C. Pei, S. Chen, J. Xie, S. Feng, M. Yu, C. Zhan, Y. Qian, G. Yang, Y. Chen, S. Lan, E. Kan, D. Wang, X. Mu, H. Hahn, B. Sun, G. Wilde, T. Feng, Strain engineering in gradient-structured metallic glasses for excellent overall water splitting, Mater. Today 85 (2025) 100–111.
[10] Y. Sun, H. Liao, J. Wang, B. Chen, S. Sun, S.J.H. Ong, S. Xi, C. Diao, Y. Du, J. O. Wang, M.B.H. Breese, S. Li, H. Zhang, Z.J. Xu, Covalency competition dominates the water oxidation structure–activity relationship on spinel oxides, Nat. Catal. 3 (2020) 554–563.
[11] J. Huang, H. Sheng, R.D. Ross, J. Han, X. Wang, B. Song, S. Jin, Modifying redox properties and local bonding of Co_3O_4 by CeO_2 enhances oxygen evolution catalysis in acid, Nat. Commun. 12 (2021) 3036.
[12] H. Wang, T. Zhai, Y. Wu, T. Zhou, B. Zhou, C. Shang, Z. Guo, High-valence oxides for high performance oxygen evolution electrocatalysis, Adv. Sci. 10 (2023) 2301706.
[13] J. Kang, X. Qiu, Q. Hu, J. Zhong, X. Gao, R. Huang, C. Wan, L.M. Liu, X. Duan, L. Guo, Valence oscillation and dynamic active sites in monolayer NiCo hydroxides for water oxidation, Nat. Catal. 4 (2021) 1050–1058.
[14] Y. Bai, Y. Wu, X. Zhou, Y. Ye, K. Nie, J. Wang, M. Xie, Z. Zhang, Z. Liu, T. Cheng, C. Gao, Promoting nickel oxidation state transitions in single-layer NiFeB hydroxide nanosheets for efficient oxygen evolution, Nat. Commun. 13 (2022) 6094.
[15] X. Zhang, Z. Li, W. Shen, G. Zhao, Z. Yi, J. Qi, C. Liang, In-situ surface-selective removal of al element from NiFeAl ternary nanowires for large-current oxygen evolution reaction, ChemNanoMat 7 (2021) 1138–1144.
[16] J. Huang, J. Han, T. Wu, K. Feng, T. Yao, X. Wang, S. Liu, J. Zhong, Z. Zhang, Y. Zhang, B. Song, Boosting hydrogen transfer during volmer reaction at oxides/metal nanocomposites for efficient alkaline hydrogen evolution, ACS Energy Lett. 4 (2019) 3002–3010.
[17] B. Li, S.D. Jiang, Q. Fu, R. Wang, W.Z. Xu, J.X. Chen, C. Liu, P. Xu, X.J. Wang, J. H. Li, H.B. Fan, J.T. Huo, J.F. Sun, Z.L. Ning, B. Song, Tailoring nanocrystalline/amorphous interfaces to enhance oxygen evolution reaction performance for FeNi-based alloy fibers, Adv. Funct. Mater. 35 (2024) 2413088.
[18] Y. Park, H.Y. Jang, T.K. Lee, T. Kim, D. Kim, D. Kim, H. Baik, J. Choi, T. Kwon, S. J. Yoo, S. Back, K. Lee, Atomic-level Ru-Ir mixing in rutile-type $(RuIr)O_2$ for efficient and durable oxygen evolution catalysis, Nat. Commun. 16 (2025) 579.
[19] N. Du, C. Roy, R. Peach, M. Turnbull, S. Thiele, C. Bock, Anion-exchange membrane water electrolyzers, Chem. Rev. 122 (2022) 11830–11895.
[20] Q. Wen, K. Yang, D. Huang, G. Cheng, X. Ai, Y. Liu, J. Fang, H. Li, L. Yu, T. Zhai, Schottky heterojunction nanosheet array achieving high-current-density oxygen evolution for industrial water splitting electrolyzers, Adv. Energy Mater. 11 (2021) 2102353.
[21] Q. Ye, L. Li, H. Li, X. Gu, B. Han, X. Xu, F. Wang, B. Li, Quasi-parallel NiFe layered double hydroxide nanosheet arrays for large-current-density oxygen evolution electrocatalysis, ChemSusChem 15 (2022) e202101873.
[22] J.W. Yeh, S.K. Chen, S.J. Lin, J.Y. Gan, T.S. Chin, T.T. Shun, C.H. Tsau, S.Y. Chang, Nanostructured high-entropy alloys with multiple principal elements: novel alloy design concepts and outcomes, Adv. Eng. Mater. 6 (2004) 299–303.
[23] T.X. Nguyen, Y.H. Su, C.C. Lin, J. Ruan, J.M. Ting, A new high entropy glycerate for high performance oxygen evolution reaction, Adv. Sci. 8 (2021) 2002446.

[24] R. Wang, J. Huang, X. Zhang, J. Han, Z. Zhang, T. Gao, L. Xu, S. Liu, P. Xu, B. Song, Two-dimensional high-entropy metal phosphorus trichalcogenides for enhanced hydrogen evolution reaction, ACS Nano 16 (2022) 3593–3603.
[25] P. Li, X. Wan, J. Su, W. Liu, Y. Guo, H. Yin, D. Wang, A single-phase FeCoNiMnMo high-entropy alloy oxygen evolution anode working in alkaline solution for over 1000h, ACS Catal. 12 (2022) 11667–11674.
[26] K. Huang, D. Peng, Z. Yao, J. Xia, B. Zhang, H. Liu, Z. Chen, F. Wu, J. Wu, Y. Huang, Cathodic plasma driven self-assembly of HEAs dendrites by pure single FCC FeCoNiMnCu nanoparticles as high efficient electrocatalysts for OER, Chem. Eng. J. 425 (2021) 131533.
[27] J. Man, B. Wu, G. Duan, L. Zhang, X. Du, Y. Liu, C. Esling, Super-high strength of a CoCrNiFe based high entropy alloy, J. Mater. Sci. Technol. 177 (2024) 79–84.
[28] R.Q. Yao, Y.T. Zhou, H. Shi, W.B. Wan, Q.H. Zhang, L. Gu, Y.F. Zhu, Z. Wen, X. Y. Lang, Q. Jiang, Nanoporous surface high-entropy alloys as highly efficient multisite electrocatalysts for nonacidic hydrogen evolution reaction, Adv. Funct. Mater. 31 (2021) 2009613.
[29] R. He, L. Yang, Y. Zhang, X. Wang, S. Lee, T. Zhang, L. Li, Z. Liang, J. Chen, J. Li, A. Ostovari Moghaddam, J. Llorca, M. Ibáñez, J. Arbiol, Y. Xu, A. Cabot, A CrMnFeCoNi high entropy alloy boosting oxygen evolution/reduction reactions and zinc-air battery performance, Energy Storage Mater. 58 (2023) 287–298.
[30] M. Han, C. Wang, J. Zhong, J. Han, N. Wang, A. Seifitokaldani, Y. Yu, Y. Liu, X. Sun, A. Vomiero, H. Liang, Promoted self-construction of β-NiOOH in amorphous high entropy electrocatalysts for the oxygen evolution reaction, Appl. Catal. B Environ. 301 (2022) 120764.
[31] H. Zhu, S. Sun, J. Hao, Z. Zhuang, S. Zhang, T. Wang, Q. Kang, S. Lu, X. Wang, F. Lai, T. Liu, G. Gao, M. Du, D. Wang, A high-entropy atomic environment converts inactive to active sites for electrocatalysis, Energy Environ. Sci. 16 (2023) 619–628.
[32] Y.F. Cui, S.D. Jiang, Q. Fu, R. Wang, P. Xu, Y. Sui, X.J. Wang, Z.L. Ning, J.F. Sun, X. Sun, A. Nikiforov, B. Song, Cost-effective high entropy core–shell fiber for stable oxygen evolution reaction at 2 a cm^{-2}, Adv. Funct. Mater. 33 (2023) 2306889.
[33] X. Zhang, Y. Yang, Y. Liu, Z. Jia, Q. Wang, L. Sun, L.C. Zhang, J.J. Kruzic, J. Lu, B. Shen, Defect engineering of a high-entropy metallic glass surface for high-performance overall water splitting at ampere-level current densities, Adv. Mater. 35 (2023) 2303439.
[34] L. Wang, L. Zhang, X. Lu, F. Wu, X. Sun, H. Zhao, Q. Li, Surprising cocktail effect in high entropy alloys on catalyzing magnesium hydride for solid-state hydrogen storage, Chem. Eng. J. 465 (2023) 142766.
[35] J. Chen, Y. Ji, Locating the cocktail and scaling-relation breaking effects of high-entropy alloy catalysts on the electrocatalytic volcano plot, Chin. J. Catal. 43 (2022) 2889–2897.
[36] H. Nan, S. Lv, Z. Xu, Y. Feng, Y. Zhou, M. Liu, T. Wang, X. Liu, X. Hu, H. Tian, Inducing the cocktail effect in yolk-shell high-entropy perovskite oxides using an electronic structural design for improved electrochemical applications, Chem. Eng. J. 452 (2023) 139501.
[37] J. Zhang, H. Zhang, Y. Huang, Electron-rich NiFe layered double hydroxides via interface engineering for boosting electrocatalytic oxygen evolution, Appl. Catal. B Environ. 297 (2021) 120453.
[38] Y. Zhai, X. Ren, T. Gan, L. She, Q. Guo, N. Yang, B. Wang, Y. Yao, S. Liu, Deciphering the synergy of multiple vacancies in high-entropy layered double hydroxides for efficient oxygen electrocatalysis, Adv. Energy Mater. 15 (2025) 2502065.
[39] Y. Mei, Y. Feng, C. Zhang, Y. Zhang, Q. Qi, J. Hu, High-entropy alloy with Mo-coordination as efficient electrocatalyst for oxygen evolution reaction, ACS Catal. 12 (2022) 10808–10817.
[40] K. Li, J. Gao, X. Han, Q. Shao, Z. Lü, Novel medium entropy perovskite oxide Sr $(FeCoNiMo)_{1/4}O_3-\delta$ for zinc-air battery cathode, J. Energy Chem. 96 (2024) 669–678.
[41] A. Asghari Alamdari, H. Jahangiri, M.B. Yagci, K. Igarashi, H. Matsumoto, A. Motallebzadeh, U. Unal, Exploring the role of mo and mn in improving the OER and HER performance of CoCuFeNi-Based High-Entropy alloys, ACS Appl. Energy Mater. 7 (2024) 2423–2435.
[42] W. Huang, A.C. Johnston-Peck, T. Wolter, W.C.D. Yang, L. Xu, J. Oh, B.A. Reeves, C. Zhou, M.E. Holtz, A.A. Herzing, A.M. Lindenberg, M. Mavrikakis, M. Cargnello, Steam-created grain boundaries for methane C–H activation in palladium catalysts, Science 373 (2021) 1518–1523.
[43] R. Li, R. Wu, Z. Li, J. Wang, X. Liu, Y. Wen, F.-K. Chiang, S.-W. Chen, K.C. Chan, Z. Lu, Boosting oxygen-evolving activity via atom-stepped interfaces architected with kinetic frustration, Adv. Mater. 35 (2023) 2206890.
[44] E. Zhu, W. Xue, S. Wang, X. Yan, J. Zhou, Y. Liu, J. Cai, E. Liu, Q. Jia, X. Duan, Y. Li, H. Heinz, Y. Huang, Enhancement of oxygen reduction reaction activity by grain boundaries in platinum nanostructures, Nano Res 13 (2020) 3310–3314.
[45] R. Chattot, O. Le Bacq, V. Beermann, S. Kühl, J. Herranz, S. Henning, L. Kühn, T. Asset, L. Guétaz, G. Renou, J. Drnec, P. Bordet, A. Pasturel, A. Eychmüller, T. J. Schmidt, P. Strasser, L. Dubau, F. Maillard, Surface distortion as a unifying concept and descriptor in oxygen reduction reaction electrocatalysis, Nat. Mater. 17 (2018) 827–833.
[46] Q. Yu, W.W. Xu, C. Cui, X. Gong, W. Li, L. Chen, X. Li, L. Vitos, Unveiling segregation-induced evolution in phase constitution of Cu-containing high-entropy alloys, J. Alloy. Compd. 843 (2020) 156109.
[47] S. Thapliyal, P. Agrawal, P. Agrawal, S.S. Nene, R.S. Mishra, B.A. McWilliams, K. C. Cho, Segregation engineering of grain boundaries of a metastable Fe-Mn-Co-Cr-Si high entropy alloy with laser-powder bed fusion additive manufacturing, Acta Mater. 219 (2021) 117271.
[48] T. Ye, Y. Wang, X. Yao, H. Li, T. Xiao, K. Ba, Y. Tang, C. Zheng, X. Yang, Z. Sun, Synthesis of rhenium-doped copper twin boundary for high-turnover-frequency electrochemical nitrogen reduction, ACS Appl. Mater. Interfaces 16 (2024) 24580–24589.
[49] T. Luo, F. Serrano-Sánchez, H. Bishara, S. Zhang, R. Bueno Villoro, J.J. Kuo, C. Felser, C. Scheu, G.J. Snyder, J.P. Best, G. Dehm, Y. Yu, D. Raabe, C. Fu, B. Gault, Dopant-segregation to grain boundaries controls electrical conductivity of n-type NbCo(Pt)Sn half-Heusler alloy mediating thermoelectric performance, Acta Mater. 217 (2021) 117147.
[50] X. Geng, M. Vega-Paredes, Z. Wang, C. Ophus, P. Lu, Y. Ma, S. Zhang, C. Scheu, C. H. Liebscher, B. Gault, Grain boundary engineering for efficient and durable electrocatalysis, Nat. Commun. 15 (2024) 8534.
[51] W. Niu, Z. Chen, W. Guo, W. Mao, Y. Liu, Y. Guo, J. Chen, R. Huang, L. Kang, Y. Ma, Q. Yan, J. Ye, C. Cui, L. Zhang, P. Wang, X. Xu, B. Zhang, Pb-rich cu grain boundary sites for selective CO-to-n-propanol electroconversion, Nat. Commun. 14 (2023) 4882.
[52] P. Lejček, S. Hofmann, M. Všianská, M. Šob, Entropy matters in grain boundary segregation, Acta Mater. 206 (2021) 116597.
[53] D. Palanisamy, S. Ener, F. Maccari, L. Schäfer, K.P. Skokov, O. Gutfleisch, D. Raabe, B. Gault, Grain boundary segregation, phase formation, and their influence on the coercivity of rapidly solidified $SmFe_{11}Ti$ hard magnetic alloys, Phys. Rev. Mater. 4 (2020) 054404.
[54] Y.H. Wang, B. Li, Y.F. Cui, Y. Du, Z.W. Yu, L.Y. Zhang, Z.L. Ning, X. Sun, J.H. Li, X. B. Tang, H. Liang, Q. Wang, E. P, J.T. Huo, G. Wang, J.F. Sun, S.D. Jiang, Catalytic mechanism of nanocrystalline and amorphous matrix in Fe-based microwires for advanced oxidation, Adv. Funct. Mater. 35 (2025) 2425912.
[55] H. Yin, Y. Huang, Y. Bao, S. Jiang, P. Xue, S. Jiang, H. Wang, F. Qin, Z. Li, S. Sun, Y. Wang, H. Shen, J. Sun, Comparable magnetocaloric properties of melt-extracted $Gd_{36}Tb_{20}Co_{20}Al_{24}$ metallic glass microwires, J. Alloy. Compd. 815 (2020) 150983.
[56] H. Schwarz, J. Apell, H.K. Wong, P. Henning, R. Wonneberger, N. Rösch, T. Uhlig, F. Ospald, G. Wagner, A. Undisz, T. Seyller, Fabrication of single-crystalline CoCrFeNi thin films by DC magnetron sputtering: a route to surface studies of high-entropy alloys, Adv. Mater. 35 (2023) 2301526.
[57] Y. Xing, C.J. Li, Y.K. Mu, Y.D. Jia, K.K. Song, J. Tan, G. Wang, Z.Q. Zhang, J.H. Yi, J. Eckert, Strengthening and deformation mechanism of high-strength CrMnFeCoNi high entropy alloy prepared by powder metallurgy, J. Mater. Sci. Technol. 132 (2023) 119–131.
[58] D. Xing, H. Shen, S. Jiang, J. Liu, M.H. Phan, H. Wang, F. Qin, D. Chen, Y. Liu, J. Sun, Magnetocaloric effect and critical behavior in melt-extracted $Gd_{60}Co_{15}Al_{25}$ microwires, Phys. Status Solidi A. 212 (2015) 1905–1910.
[59] S. Jiang, G. Cao, Z. Jia, L. Sun, C. Wang, H. Fan, Y. Wang, W. Xu, Y. Cui, Z. Ning, J. Sun, J. Li, X. Tang, H. Liang, E. Peng, A superb iron-based glassy-crystal alloy fiber as an ultrafast and stable catalyst for advanced oxidation, Adv. Fiber Mater. 6 (2024) 1483–1494.
[60] S. Jiang, H. Wang, D. Estevez, Y. Huang, L. Zhang, H. Shen, Z. Ning, F. Qin, J. Sun, Surface microstructural design to improve mechanical and giant magneto-impedance properties of melt-extracted CoFe-based amorphous wires, Mater. Des. 204 (2021) 109642.
[61] H. Wang, F.X. Qin, D.W. Xing, F.Y. Cao, X.D. Wang, H.X. Peng, J.F. Sun, Relating residual stress and microstructure to mechanical and giant magneto-impedance properties in cold-drawn Co-based amorphous microwires, Acta Mater. 60 (2012) 5425–5436.
[62] Y. Bao, H. Shen, D. Xing, S. Jiang, J. Sun, M.-H. Phan, Enhanced curie temperature and cooling efficiency in melt-extracted $Gd_{50}(Co_{69.25}Fe_{4.25}Si_{13}B_{13.5})_{50}$ microwires, J. Alloy. Compd. 708 (2017) 678–684.
[63] J. Liu, Z. Du, S. Jiang, H. Shen, Z. Li, D. Xing, W. Ma, J. Sun, Tailoring giant magnetoimpedance effect of Co-based microwires for optimum efficiency by self-designed square-wave pulse current annealing, J. Magn. Magn. Mater. 385 (2015) 145–150.
[64] J. Liang, G. Cao, M. Zeng, L. Fu, Controllable synthesis of high-entropy alloys, Chem. Soc. Rev. 53 (2024) 6021–6041.
[65] G. Kresse, J. Furthmüller, Efficient iterative schemes for ab initio total-energy calculations using a plane-wave basis set, Phys. Rev. B. 54 (1996) 11169–11186.
[66] J.P. Perdew, K. Burke, M. Ernzerhof, Generalized gradient approximation made simple, Phys. Rev. Lett. 77 (1996) 3865–3868.
[67] J.K. Nørskov, J. Rossmeisl, A. Logadottir, L. Lindqvist, J.R. Kitchin, T. Bligaard, H. Jónsson, Origin of the overpotential for oxygen reduction at a fuel-cell cathode, J. Phys. Chem. B. 108 (2004) 17886–17892.
[68] L. Banko, O.A. Krysiak, J.K. Pedersen, B. Xiao, A. Savan, T. Löffler, S. Baha, J. Rossmeisl, W. Schuhmann, A. Ludwig, Unravelling composition–activity–stability trends in high entropy alloy electrocatalysts by using a data-guided combinatorial synthesis strategy and computational modeling, Adv. Energy Mater. 12 (2022) 2103312.
[69] C. Wen, Y. Zhang, C. Wang, D. Xue, Y. Bai, S. Antonov, L. Dai, T. Lookman, Y. Su, Machine learning assisted design of high entropy alloys with desired property, Acta Mater. 170 (2019) 109–117.
[70] G.L.W. Hart, T. Mueller, C. Toher, S. Curtarolo, Machine learning for alloys, Nat. Rev. Mater. 6 (2021) 730–755.
[71] J.K. Pedersen, T.A.A. Batchelor, A. Bagger, J. Rossmeisl, High-entropy alloys as catalysts for the CO_2 and CO reduction reactions, ACS Catal. 10 (2020) 2169–2176.
[72] J. Hu, Y.N. Shi, X. Sauvage, G. Sha, K. Lu, Grain boundary stability governs hardening and softening in extremely fine nanograined metals, Science 355 (2017) 1292–1296.
[73] K.N. Campo, C.C. de Freitas, L. Fanton, R. Caram, Melting behavior and globular microstructure formation in semi-solid CoCrCuxFeNi high-entropy alloys, J. Mater. Sci. Technol. 52 (2020) 207–217.

[74] J. Su, Y. Yang, G. Xia, J. Chen, P. Jiang, Q. Chen, Ruthenium-cobalt nanoalloys encapsulated in nitrogen-doped graphene as active electrocatalysts for producing hydrogen in alkaline media, Nat. Commun. 8 (2017) 14969.
[75] W. Xu, G. Fan, S. Zhu, Y. Liang, Z. Cui, Z. Li, H. Jiang, S. Wu, F. Cheng, Electronic structure modulation of nanoporous cobalt phosphide by carbon doping for alkaline hydrogen evolution reaction, Adv. Funct. Mater. 31 (2021) 2107333.
[76] H.B. Tao, Y. Xu, X. Huang, J. Chen, L. Pei, J. Zhang, J.G. Chen, B. Liu, A general method to probe oxygen evolution intermediates at operating conditions, Joule 3 (2019) 1498–1509.
[77] N. Zhang, X. Feng, D. Rao, X. Deng, L. Cai, B. Qiu, R. Long, Y. Xiong, Y. Lu, Y. Chai, Lattice oxygen activation enabled by high-valence metal sites for enhanced water oxidation, Nat. Commun. 11 (2020) 4066.
[78] Y. Yang, Y. Qian, Z. Luo, H. Li, L. Chen, X. Cao, S. Wei, B. Zhou, Z. Zhang, S. Chen, W. Yan, J. Dong, L. Song, W. Zhang, R. Feng, J. Zhou, K. Du, X. Li, X.M. Zhang, X. Fan, Water induced ultrathin Mo2C nanosheets with high-density grain boundaries for enhanced hydrogen evolution, Nat. Commun. 13 (2022) 7225.
[79] Y. Li, Y. Wu, M. Yuan, H. Hao, Z. Lv, L. Xu, B. Wei, Operando spectroscopies unveil interfacial FeOOH induced highly reactive β-Ni(Fe)OOH for efficient oxygen evolution, Appl. Catal. B Environ. 318 (2022) 121825.
[80] I. Georgiou, S. Kervyn, A. Rossignon, F.De Leo, J. Wouters, G. Bruylants, D. Bonifazi, Versatile self-adapting boronic acids for h-bond recognition: from discrete to polymeric supramolecules, J. Am. Chem. Soc. 139 (2017) 2710–2727.
[81] F. Song, L. Bai, A. Moysiadou, S. Lee, C. Hu, L. Liardet, X. Hu, Transition metal oxides as electrocatalysts for the oxygen evolution reaction in alkaline solutions: an application-inspired renaissance, J. Am. Chem. Soc. 140 (2018) 7748–7759.
[82] W. Shi, J. Zhu, L. Gong, D. Feng, Q. Ma, J. Yu, H. Tang, Y. Zhao, S. Mu, Fe-Incorporated Ni/MoO_2 hollow heterostructure nanorod arrays for high-efficiency overall water splitting in alkaline and seawater media, Small 18 (2022) 2205683.
[83] Z. Wang, S. Shen, J. Wang, W. Zhong, Modulating the d-band center of electrocatalysts for enhanced water splitting, Chem. Eur. J. 30 (2024) e202402725.